Assessment of ERA5 Near-Surface Air Temperatures Over Global Oceans by Combining MODIS Sea Surface Temperature Products and In-Situ Observations

Min He , Jun Qin , Ning Lu , and Ling Yao

Abstract—European Centre for Medium-Range Weather Forecasts Reanalysis 5 (ERA5) is a state-of-the-art reanalysis dataset and has been widely used in climate change analysis and land surface process simulations. However, few assessments have been conducted across the entire ocean for this dataset till now. The motivation of this study is to utilize the in-situ observations and remotely sensed sea surface temperature (SST) products to propose a new approach to evaluate the precision of ERA5 air temperature over the whole ocean. First, a stacked multilayer perceptron regressor model was employed to map global marine air temperature (MAT) by incorporating in-situ records into moderate-resolution imaging spectroradiometer (MODIS) SST products. Second, a monthly MAT dataset with a spatial resolution of $0.05° \times 0.05°$ was developed and validated for the assessment of ERA5 air temperature particularly in the regions where only satellite observations are available. It demonstrates that the quality of estimated MAT (RMSE = 1.62 °C, Bias = 0.03 °C) is evidently high in 80.3% of the observation stations, which is much better than that of averaged SST (RMSE = 2.29 °C, Bias = 1.14 °C). Thus, the estimated MAT is credible enough to be employed to assess ERA5 air temperature both at the grid and regional scale. Finally, the ERA5 air temperature was compared and validated with the estimated MAT temporally and spatially. The further study suggested that estimated MAT and ERA5 air temperature basically maintain consistency in expressing persistent warming, particularly in the western Pacific, western Atlantic, and northern Indian Ocean. In addition, the trend of ERA5 air temperature during 50°S–50°N reaches 0.016 ± 0.003°C/yr, which is similar to that of estimated MAT (0.017 ± 0.002 °C/yr) during 2003–2021.

Index Terms—European Centre for Medium-Range Weather Forecasts Reanalysis 5 (ERA5), machine learning, marine air temperature (MAT), MODIS, sea surface temperature (SST), warming trend.

Min He is with the State Key Laboratory of Resources and Environmental Information System, Institute of Geographic Sciences and Natural Resources Research, Chinese Academy of Sciences, Beijing 100101, China, and also with the College of Resources and Environment, University of Chinese Academy of Sciences, Beijing 100049, China (e-mail: minhe5799@gmail.com).

Jun Qin, Ning Lu, and Ling Yao are with the State Key Laboratory of Resources and Environmental Information System, Institute of Geographic Sciences and Natural Resources Research, Chinese Academy of Sciences, Beijing 100101, China (e-mail: qinjun@igsnrr.ac.cn; lvn@lreis.ac.cn; yaoling@lreis.ac.cn).

Digital Object Identifier 10.1109/JSTARS.2023.3312810

I. INTRODUCTION

OCEANS cover about 71% of the Earth's surface and serve as a vast heat reservoir globally [1], [2]. The existing research has proved that the ocean's heat capacity can cause a lag of up to 2 °C in CO_2-induced global warming [3]. The marine air temperature (MAT) is not only important to the marine ecosystem but also a crucial driver of atmospheric movements and ocean current movement [4]. Therefore, the warming assessment of the ocean is quite essential to global temperature change. However, due to the scarcity and inconsistency of in-situ climate records over the oceans, it is difficult to obtain an accurate assessment of global ocean warming [5], [6]. Previous studies have generally employed sea surface temperature (SST) as a proxy for MAT, either implicitly or explicitly, when investigating ocean temperature anomalies [7], [8], [9]. Alternatively, some studies only take night MAT (NMAT) as a substitute for all-day air temperature to evaluate global temperature anomaly [10]. Nevertheless, as questioned in other studies, SST is different from MAT or NMAT in terms of physical properties and long-term climatology variability and trends [5], [11], [12], particularly in the tropical Pacific Ocean [13]. Therefore, an homogenous MAT dataset is demanded for obtaining unbiased assessments on global warming both in the past and future [14].

Current MAT products mainly include International Comprehensive Ocean-Atmosphere Data Set (ICOADS) [15], [16], European Centre for Medium-Range Weather Forecasts Reanalysis 5 (ERA5) [17], North American Regional Reanalysis (NARR) [18], the Hadley Centre Night-Time MAT (HadNMAT2) [10], and others. ICOADS is the most comprehensive and continuously updated archive of global marine surface climate observations, containing monthly statistical summaries from 1800 to the present for each $2° \times 2°$ area. The majority of the records have been collected by ships-of-opportunity, supplemented in recent years by research vessels, moored environmental buoys, drifting buoys, and hydrographic profiles. However, the ICOADS data have not been corrected to account for biases resulting from

TABLE I
INFORMATION OF AVAILABLE SST PRODUCTS

Type	Product ID	Agency	Spatial Resolution	Coverage Range
In situ observations	ERSST	National Oceanic and Atmospheric Administration	2°×2°	1854− present
	HadSST	Met Office Hadley Centre	5°×5°	1850− present
	COBE-SST	Japan Meteorological Agency	1°×1°	1850− present
Satellite-based SST	CCI SST	European Space Agency	0.05°×0.05°	1981− present
	MODIS SST	NASA	4 km×4 km	2000− present
	AMSR2 SST	Japan Aerospace Exploration Agency	25 km×25 km	2012− present
Combined SST	HadISST	Met Office Hadley Centre	1°×1°	1871− present
	WOISST	National Centers for Environmental Prediction	1°×1°	1981− present
	DOISST	National Centers for Environmental Information	0.25°×0.25°	1981− present
	GMPE	Group for High Resolution SST	0.25°×0.25°	1981− present
	MURSST	Chin *et al*. 2017	0.01° ×0.01°	2002− present
	OSTIA	Met Office Hadley Centre	0.05°×0.05°	1981− present

instrumentation, observing practices, ship types, etc. To address these issues, HadNMAT and improved version HadNMAT2 were produced using reduced space optimal interpolation, which homogenized the observational standards [10]. HadNMAT2 is available on a 5° × 5° grid from 1880, presented as anomalies relative to the 1961–1990 calendar-monthly climatological average of night-time MAT. Another type of dataset called reanalysis datasets is generated by assimilating observed data into a physical model. Datasets, such as ERA5, covering the Earth on a 30-km grid [17] and NARR covering it on a 32-km grid [18], are widely used in series of research works. However, this type of dataset is highly dependent on the accuracy of in-situ observations and parameterizations. As it is well known, the fixed stations are sparsely and unevenly distributed on the ocean. The site-based validation can only express the accuracy for site-located grids but not yet for other grids [19], [20]. Therefore, it is hard to quantify the uncertainties over none-site-located grids in the reanalysis datasets. The comprehensive verifications by indirect means are still demanded at those regions where observation is lacking.

Remotely sensed observations have a significant advantage in spatial coverage compared with site-based observations. However, air temperature cannot be measured by satellite directly while in contrast SST is accessible [21], [22]. Typically, MAT is defined as the temperature of the near-surface layer above the sea (in the range of 1.5–5 m above the sea), whereas SST is defined as the temperature of the shallow water in the ocean. Due to their proximity, MATs and SSTs are closely linked through the process of heat flux exchange and atmospheric turbulence [13], [23]. On land, many studies have proved that there is a strong relationship between land surface temperature (LST) and near-surface air temperature due to the exchange of sensible and latent heat fluxes, which is particularly dependent on the land surface types and topographic conditions [24], [25], [26]. Currently, many researches have produced dozens of near-surface air temperature products successfully with LST

products through a variety of methods, such as geographically weighted regression, machine learning, deep neural networks, and others [27], [28], [29]. These works provide a feasible reference for MAT estimation with SSTs.

With advances in multidimensional monitoring networks, there are three types of global SST products available for climate research [30], which are listed in Table I in detail. The first type of data is interpolated by in-situ observations obtained from ships, drifting buoys, and moored buoys, including the extended reconstructed SST (ERSST), Met Office Hadley Centre SST (HadSST) [31], and Centennial Observation-Based Estimates of SSTs (COBE-SST) [32]. This type of SST is mostly characterized with a long-time history and coarse spatial resolution. The second type is merely derived from satellite observations. The thermal infrared satellite data (with transmittance depth less than 1-mm beneath water) and passive microwave satellite data (with transmittance depth near 10-m beneath water) are commonly used to obtain SST products, such as the climate change initiative SST (CCI SST), moderate-resolution imaging spectroradiometer (MODIS) SST [22], and AMSR2 SST [33], [34], [35]. Since the 1980s, satellite-based SST algorithms have been well developed [36], and significant improvements have been made in the aspects of spatial-temporal resolution and precision [37]. The third type of SST products combines both in-situ and satellite observations, such as the Met Office Hadley Centre Ice and SST (HadISST) [38], Weekly Optimum Interpolation SST (WOISST) [39], Daily Optimum Interpolation SST, version 2.0 (DOISST v2.0) [40], Multiproduct Ensemble (GMPE) SST product from the Group for High Resolution SST [41], [42], the Operational Sea Surface Temperature and Ice Analysis (OSTIA) system produced SST [43], and the multiscale ultrahigh resolution SST (MURSST) [44]. Among these products, MODIS SST has a high level of accuracy [37], [45], [46], and is able to generate global MAT products with higher spatial and temporal resolution and finer granularity.

ERA5 is the fifth generation European Centre for Medium-Range Weather Forecasts atmospheric reanalysis of the global climate, covering the period from January 1940 to present and providing hourly and monthly estimates of a large number of atmospheric, land, and oceanic climate variables [17], [47]. The data cover the Earth on a 30-km (0.1°) grid and resolve the atmosphere using 137 levels from the surface up to a height of 80 km. As one of the most state-of-the-art datasets for climate variables, ERA5 air temperature has been validated by numerous scholars and then widely used in many studies related to climate change and land surface process simulation on the ocean [19], [20]. Presently, the station-based validation is the most utilized method that conducted directly to evaluate the accuracy of ERA5 air temperature. Several observation platforms, such as manned weather stations, automatic weather stations, and buoys, are deployed on varied landcovers to gather the in-situ records for ERA5 variable validation [48], [49], [50], [51], [52]. Sometimes to reduce the uncertainties caused by scale effect, statistical downscaling or model downscaling of the reanalyzed dataset was performed during validation [53], [54], [55]. Besides, the intercomparisons between some air temperature products are conducted for the assessment of ERA5 air temperature [27], [56], [57]. However, most of the aforementioned assessments are conducted against in-situ records on the site-located land areas, whereas few studies concentrate on those oceanic areas without any stations. In this study, we further investigated and evaluated the accuracy of ERA5 air temperature over the entire ocean. For this objective, a global MAT dataset was primarily produced by machine learning model to assess the accuracy of ERA5 at both the grid and global scale. So, the rest of the article is organized as follows. The description and preprocessing of corresponding dataset, such as meteorological data and satellite-based SST products, are introduced in Section II. Then, a stacked multi-layer perceptron (MLP) model was trained by grouped dataset derived from in-situ MAT records and MODIS SST products to produce long time-series datasets of MATs, which is described in Section III. Besides, the testing and validation were conducted for estimated time-series MATs so as to serve as a credible reference for ERA5 air temperature dataset, which are discussed in Section IV. Finally, Section V concludes this article.

II. DATA DESCRIPTION

A. Description of MODIS SST

The monthly MODIS SST products employed in this study were downloaded from the Ocean Color Web operated by the National Aeronautics and Space Administration (NASA) (https://oceancolor.gsfc.nasa.gov/). There are four SST datasets derived from MODIS sensors at four moments of satellite transit, including day and night. In this study, both daytime and nighttime SST products were utilized to estimate global MAT. The original spatial resolution of MODIS SST is 4 km. However, to maintain the resolution consistency with other climatic variables, it has been regridded to a spatial resolution of 0.05° × 0.05° in this research. MODIS SST represents the skin temperature at a water depth of less than 1 mm [58], which is based on a modified version of the nonlinear SST algorithm
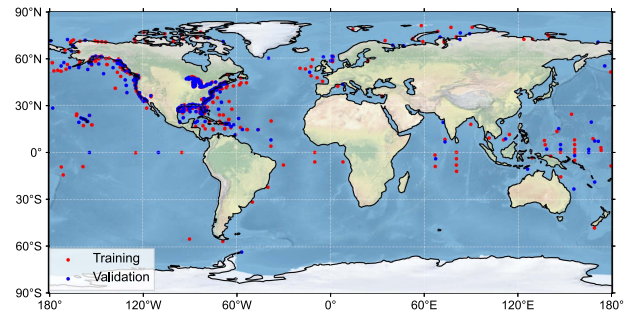

Fig. 1. Distribution of meteorological stations and buoys for MAT observations. Red dots indicate that observed MATs are used for training and blue dots are used for validation.
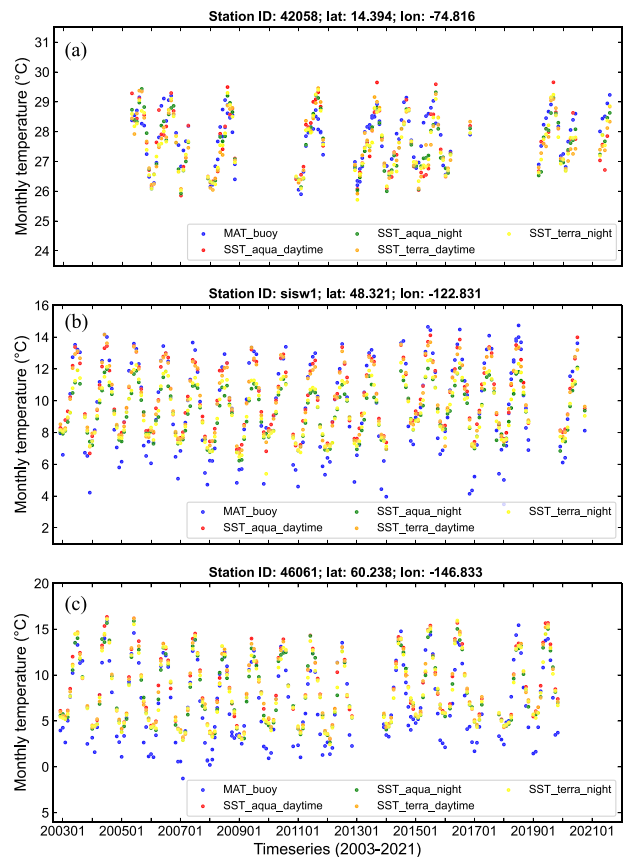

Fig. 2. Long-term observations from buoys and satellites after quality control in (a) station "42058," (b) station "sisw1," and (c) station "46061."

[22]. It is derived from the 11- and 12-µm spectral bands, as the long-wave infrared band is not susceptible to solar radiation during the day. The validations have confirmed that the average accuracy of MODIS SST product is less than 0.85 °C [59].

B. Meteorological MAT Observation

The monthly mean in-situ MATs used in this research were obtained from the National Data Buoy Center (NDBC) at website https://www.ndbc.noaa.gov/, and the National Centers for Environmental Information (NCEI) at website https://www.ncei.noaa.gov/. As a part of the National Oceanographic
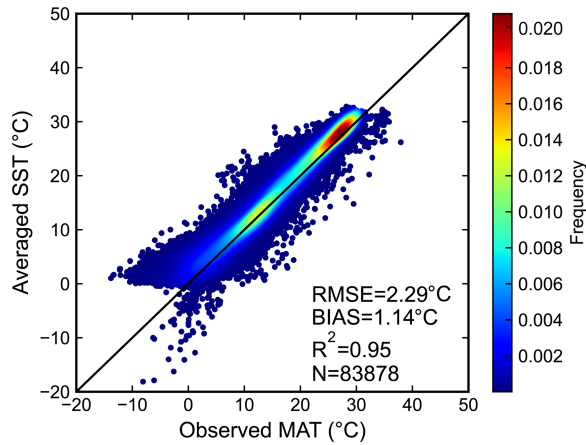
Fig. 3. Scatter plot of in-situ MATs and averaged SSTs.
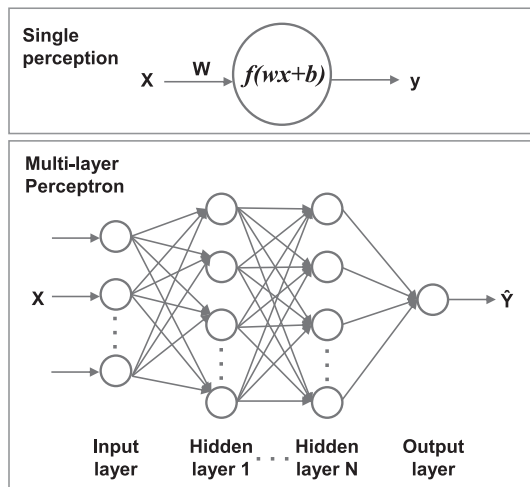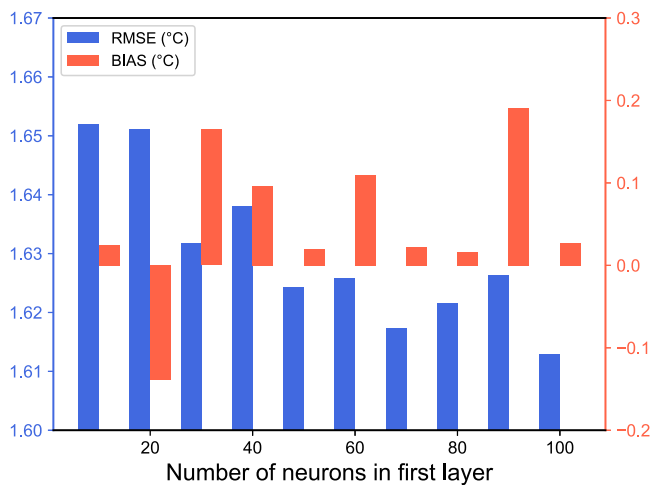

Fig. 4. Framework of MLP.

Fig. 5. Experiment result of neurons for the first layer.

and Atmospheric Administration's National Weather Service, NDBC operates and produces quality-controlled data from more than 100 moored buoys, 50 Coastal-Marine Automated Network stations, 55 Tropical Atmosphere Ocean (TAO) stations, and 39 Deep-Ocean Reporting and Assessment of Tsunamis tsunameter stations. Also, records from other stations belonging to various administrations and institutes were also collected and processed by NDBC. In contrast, NCEI merely provides the observational records from weather stations near the equator. As shown in Fig. 1, the meteorological stations and buoys used in this study are mainly located on the west and east coasts of America, Canada, the Gulf of Mexico, and the central Pacific and equatorial regions. Statistically, there are 908 sites for training, including 57 675 data records and 390 sites for testing, including 26 203 data records in total.

C. ERA5 Air Temperature Dataset

ERA5 air temperature dataset is a series of advanced global weather datasets produced by the European Centre for Medium-Range Weather Forecasts. The dataset provides hourly and monthly air temperature data over the global ocean with a spatial resolution of $0.25° \times 0.25°$ originally. It includes data from multiple sources, including satellites, radiosondes, and weather stations. The ERA5 dataset is widely used in climate research, meteorology, and environmental monitoring, as it provides a comprehensive and detailed picture of global weather patterns. In this study, monthly ERA5 air temperature dataset is regridded to $0.05° \times 0.05°$ to keep consistency with the estimated MAT product in spatial resolution.

D. In-Situ MAT Data Preprocessing

Observations derived from fixed buoys and stations always serve as the true values in engineering applications, climate research, and air–sea interaction studies. According to the reports of NDBC, the hourly validation results of employed in-situ observations expressed an average accuracy of $0.09°C$. However, the physical position of temperature sensors can adversely affect observed results. For example, nonrepresentative readings derived from complex meteorological conditions can disturb the precision of MAT over long-time observations. Therefore, it is essential to examine and control the quality of in-situ records. Here, daily MATs were examined by removing the extreme outliers. The criteria and principles of outliers mainly refer to that of TAO program conducted by Pacific Marine Environmental Laboratory. It would be marked as an outlier if: first, daily MAT changes exceed $5°C$ compared with previous day; and second, the differences between monthly MAT and mean SST exceed $15°C$. Eventually, more than 80 000 pairs of monthly MAT records during 2003–2021 are available after quality control. Here, three sites at varied latitude zones are exemplified in Fig. 2. The deviations between MAT and SST are smaller at low-latitude zone [see Fig. 2(a)] than that at mid-latitude [see Fig. 2(b) and high-latitude zone and Fig. 2(c)]. In other words, SST is not equivalent to MAT in terms of numerical value except
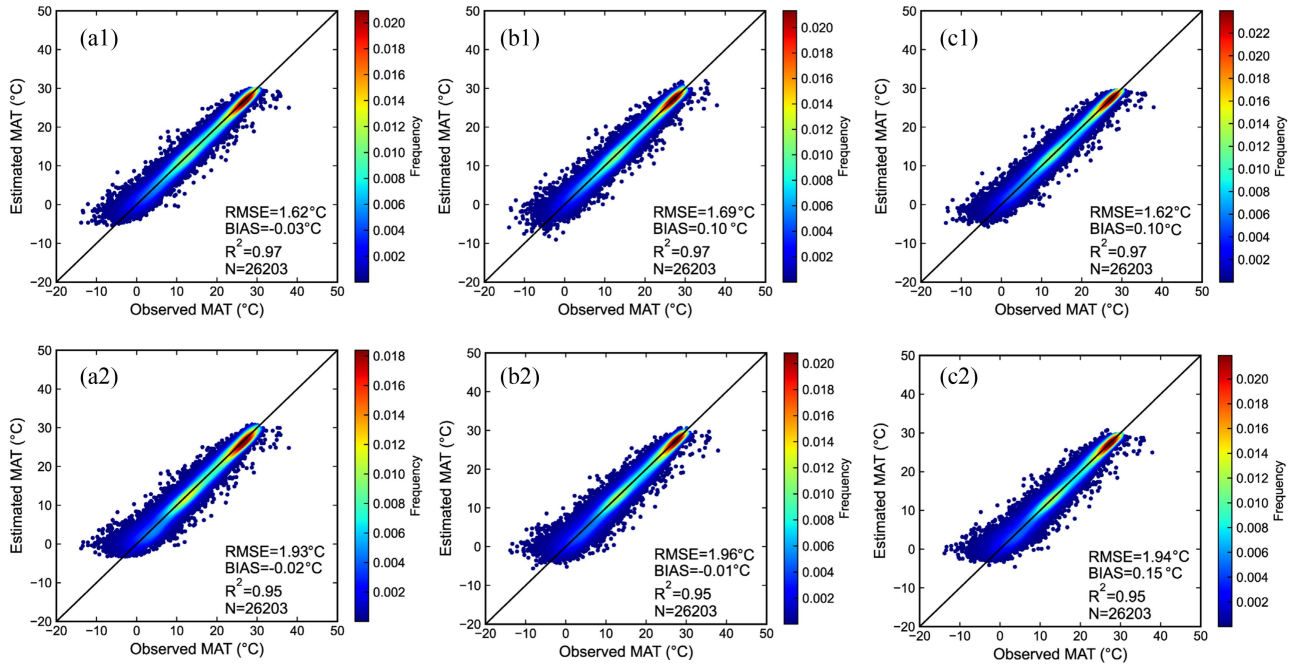
Fig. 6.   Scatter plots of the observed MAT and estimated MAT from (a1 and a2) MLP, (b1 and b2) RF, and (c1 and c2) cubist. In (a1–c1), cosine of SZA was incorporated into models, whereas in (a2–c2), it was not.

at low latitudes. Furthermore, the large differences between SST in daytime and in nighttime mainly occurred in the mid-latitude regions [see Fig. 2(b)], highlighting the heterogeneity between SST and MAT at specific occasions. As shown in Fig. 3, the mean BIAS between in-situ MAT and average SST is up to 1.14 °C. And in hot area or month, the amplitude of MAT is smaller than that of SST. In cold area, the minimum MATs are far below −10 °C, which is much lower than that of SST. Anyway, the relationship between SST and MAT is not stable in different regions, which is the main reason for this study.

E. Other Ancillary Data

Considering the radiation heterogeneity at varied regions, the angular information of the sun will also be incorporated into the stacked model. It is well known that solar radiation is the primary source of energy for the ocean, which has a strong impact on SST. Thus, the solar zenith angle (SZA), serving as the main factor of radiation heterogeneity, is an essential variable to this research.

III. METHODOLOGY

In most cases, a single model cannot overcome all the problems caused by the quality and size of training dataset. The theory of ensemble learning aims to obtain a better and more comprehensive strongly supervised model by combining multiple weakly supervised models. The goal of ensemble learning is to output a correct prediction even if one of the weak models generates a wrong prediction. In this study, a stacked model trained by MLP model was employed to estimate global MAT based on the theory of ensemble learning for the reason of geography-related phenomena in global air temperature.

A. Multilayer Perceptron

MLP is a supplement of feedforward neural network, which can be used to approximate any continuous function. It consists of multiple layers of interconnected nodes or neurons, including the input layer, output layer, and hidden layer, as is pointed out in Fig. 4. The input layer receives the input variables, whereas the required task, such as prediction and classification, is performed by the output layer. An arbitrary number of hidden layers, located between the input and output layers, serve as the true computational engine of the MLP. The neurons in each layer are called perceptions, which are controlled by activation function when working. As pointed in Fig. 4, a single perceptron receives h features as input ($\mathbf{X} = x1, x2, \ldots, xh$), and each of these features is associated with a weight coefficient ($\mathbf{W} = w1, w2, \ldots, wh$). Under the control of activation function (ϕ), the output of hidden layer H can be written as

$$H = \phi\left(XW_h + b_h\right). \tag{1}$$

Then, the input of the next layer derives from the output of the previous layer. And ultimately the output (O) of the neural network with the constraint of proposed loss function C can be expressed as follows:

$$O = \phi\left(HW_0 + b_0\right) \tag{2}$$

here, a loss function (also called error function) is used to measure the variations between the actual output a^L of the neural network and the correct output y. In this study, we used the simple and intuitive mean-squared-error loss function, which
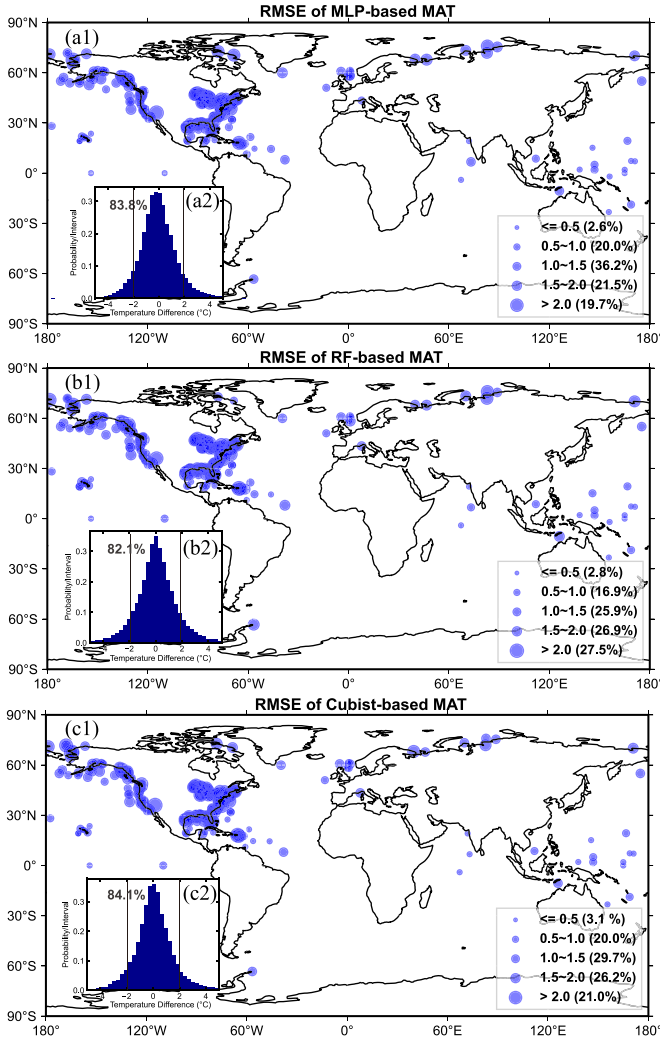
Fig. 7. Map of the RMSEs (°C) for (a) MLP, (b) RF, and (c) cubist and corresponding histogram of differences between in-situ observations and estimated results.

can be written as

$$C = \frac{1}{2} \|a^L - y\|_2^2. \tag{3}$$

The neurons in the MLP are trained by the back propagation learning algorithm. MLPs are designed to approximate any continuous function and can solve those problems that are not linearly separable.

B. Ensemble Learning

In this study, we split the paired observation dataset into training (70%) and testing (30%) sets. And as the key input variables, SST and cosine of SZA are employed to train MAT estimation model. To account for the impact of the missing values caused by cloud contamination, two stacked learning models were ensembled to obtain MAT. First, an MLP model f_{MLP1} was trained to calculate the corresponding MAT for individual product by SST product, which can be abbreviated as

$$MAT_i = f_{MLP1} \ (SST_i, \ CosSZA) \tag{4}$$

where i ($i = 12,34$) stands for the ith SST product referring to SST from Aqua and Terra in the daytime and at night, respectively. And after that, the second model f_{MLP2} was trained to obtain the final MAT. The simplified expression of the second model can be abbreviated as

$$MAT \ = f_{MLP2} \ (MAT_1, \ MAT_2, MAT_3, MAT_4) . \tag{5}$$

In this article, we trained a two-layer MLP model with ReLU activation function and adaptive learning rate. To test the impact of the number of neurons in the first layer, a control experiment is conduct. As shown in Fig. 5, the RMSEs are slightly different, whereas the BIASs are obviously divergent when the neurons are changing. When the first layer is composed of 100 neurons, the RMSE and BIAS indicate a good performance of the MLP model. Eventually, the first layer is made of 100 neuros and the second layer has 10 neuros in the MLP model training. Besides, we set the maximum number of iterations with the default value (i.e., 200) and employed the Adam optimizer for weight optimization.

IV. RESULTS AND DISCUSSION

A. Assessment of Estimated Results

1) Overall Performance of Ensemble Learning: In this study, MLP is chosen to estimate MAT mainly for the reason of continuous geography-related phenomena. However, to test the efficiency of MLP in a credible way, the random forest (RF) and Cubist model are also employed to estimate MAT due to the advances of unbiased estimates. RF can generally produce unbiased results by integrating multiple decision trees through the theory of ensemble learning [60]. And, Cubist is a rule-based model extended from Quinlan's M5 model tree [61], which works by several linear regression models at each step of a tree. Both RF and Cubist have been successfully applied in many studies to convert LSTs to SATs [60], [62]. However, the size and characteristics of the training set determine the type of estimation model. After testing, we found that it may produce discontinuous stripes when mapping global MAT with discrete models. Therefore, continuous model, such as neural network model, is the primary choice for the global map in cases where continuous and representative in-situ observations are lacking.

To appraise crudely whether or not the solar information could influence the accuracy of estimated MATs, two groups of experiments are conducted in this section. In detail, both SSTs and SZAs were considered in the first group [see Fig. 6(a1)–(c1)], whereas only SSTs were considered in the second group [see Fig. 6(a2)–(c2)]. From the view of model type, the differences caused by MLP, RF, and Cubist are quite subtle with the same parameters considered. For example, the RMSEs of MLP, RF, and Cubist are 1.62 °C, 1.69 °C, and 1.62 °C in Fig. 6(a1)–(c1), respectively. Similar results are exhibited in Fig. 6(a2)–(c2) likewise. However, from the perspective of variables, RMSEs in Fig. 6(a1)–(c1) with considering SZAs perform better than that in Fig. 6(a2)–(c2). Most importantly, the precision of MATs in cold range has been generally improved after accounting for the contribution of solar angles in Fig. 6(a1)–(c1). This improvement possibly benefits from the reduced impact of the
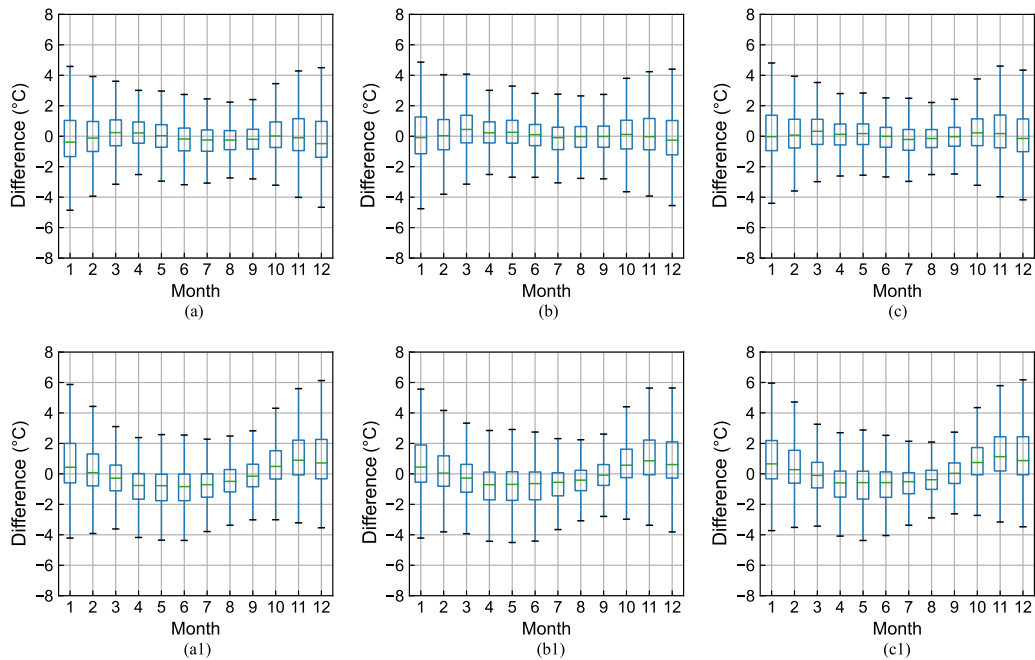
Fig. 8.   Box plots of the differences between in-situ MATs and estimated MATs from (a1 and a2) MLP, (b1 and b2) RF, and (c1 and c2) cubist. In (a1–c1), cosine of SZA was incorporated into models, whereas in (a2–c2), it was not.

bidirectional reflectance effect of the seawater. It is well known that directional radiation can conduct the distribution of solar energy [63]. It follows that the information of SZA is quite sensitive to the MAT estimates.

The uncertainty of each validation station is also crucial to the understanding of model performance. Also, to quantify and appraise the accuracies of satellite-based MAT at specific stations, the RMSEs of MLP, RF, and Cubist were mapped in Fig. 7(a1)–(c1), along with histograms of corresponding differences between all of the in-situ and satellite-based MATs [see Fig. 7(a2)–(c2)]. As is exhibited in Fig. 7(a2)–(c2), the main differences between in-situ observations and estimated results are within the range of $-2\,°C$–$2\,°C$, which confirms the overall credibility of estimated MATs to some degree. In addition, the precision of MLP-based MATs with 80.3% validation stations located within the RMSE range of $0.5\,°C$–$2\,°C$ [see Fig. 7(a1)–(c1)] outperformed that of Cubist-based (79%) and RF-based MATs (72.5%). The maximum RMSE was found near the coastlines of North America and the Arctic Coast of Russia, whereas the minimum RMSE was located in low-altitude regions $(0°$–$30°N)$ far from the mainland. There are probably two factors to influence the accuracy of MATs at specific stations. One is the land cover mixture of the grid near the shore, and the other is the short observation period less than two years for some stations. The backgrounds of a few meteorological stations (including buoys) deployed along the coast are most likely covered by both ocean and land at a grid scale of $0.05°$. In cold seasons, the grids with land and water mixed may have larger uncertainties. However, the influence of land tends to exist in the stations in mixed grid near the shore, whereas it is never existing in the stations merely located in water grid. As exhibited in Fig. 7(a1)–(c1), the validations for those stations far from the

mainland represent a higher accuracy in Fig. 7(a1)–(c1). Combining the results of Fig. 7(a2)–(c2), it has shown a holistic reliability of the satellite-derived MATs.

2) Temporally Assessment of the Model Performance: The differences between MLP-based MATs and in-situ MATs are presented in Fig. 8 to compare and assess the precision of estimated MATs in specific month. Overall, the difference is much smaller in Fig. 8(a1)–(c1) than that in Fig. 8(a2)–(c2) due to the incorporation of SZAs. In Fig. 8(a2)–(c2), the significant overestimation nearly happens in January, February, September, November, and December, whereas the underestimation mainly happens in April to October. It is probably influential in the accuracy of seasonal trend for ocean warming. In contrast, the medians of the differences in all months are close to zero in Fig. 8(a1)–(c1), which suggests that the most of the estimated MATs are unbiased compared with in-situ MATs. In addition, the differences between April and September are smaller than in other months probably due to the more uniform radiation received by the Earth during these months. In conclusion, the nuanced distinctions between the results obtained using MLP, RF, and Cubist methods provide evidence that MLP is effective in estimating monthly MAT.

3) Spatially Assessment of the Model Performance: Fig. 9 exhibits the difference map on a global scale between MLP-based MATs and averaged SSTs (abbreviated as "4SSTavg") for specific month. As shown in Fig. 9, estimated MATs are lower than 4SSTavg in most proportion of ocean except high-latitude regions, and specific areas, such as the West Coast of Africa or South America, in all months. The minimal difference mainly occurs in low-latitude regions near the equator, whereas the maxim difference generally occurs in high-latitude regions. Besides, the difference is latitude-dependent that characterized
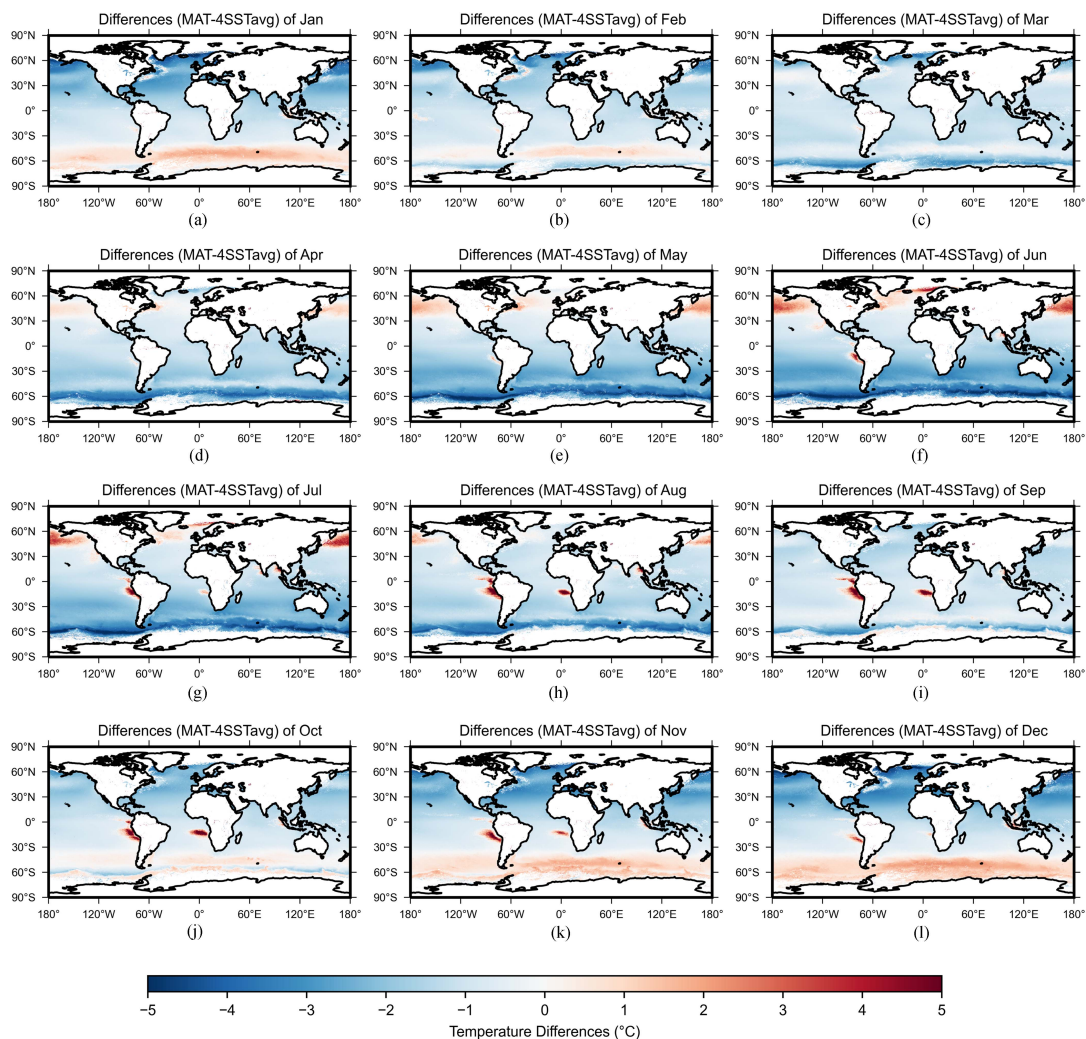
Fig. 9. Difference of average MAT and SST of 2003–2021 for specific month. (a) Differences (MAT-4SSTavg) of January. (b) Differences (MAT-4SSTavg) of February. (c) Differences (MAT-4SSTavg) of March. (d) Differences (MAT-4SSTavg) of April. (e) Differences (MAT-4SSTavg) of May. (f) Differences (MAT-4SSTavg) of June. (g) Differences (MAT-4SSTavg) of July. (h) Differences (MAT-4SSTavg) of August. (i) Differences (MAT-4SSTavg) of September. (j) Differences (MAT-4SSTavg) of October. (k) Differences (MAT-4SSTavg) of November. (l) Differences (MAT-4SSTavg) of December.
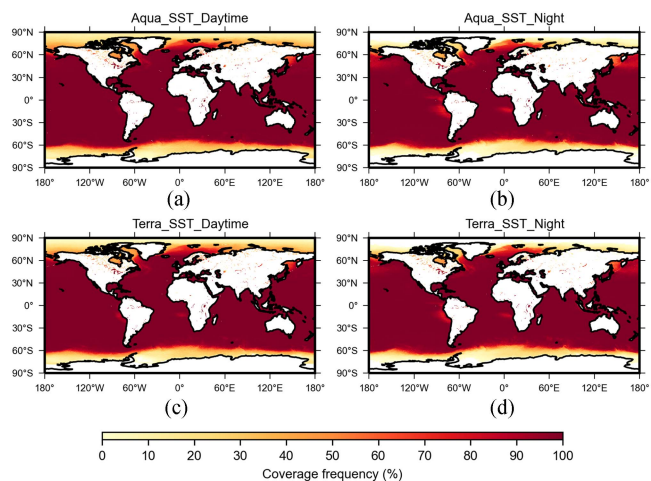

Fig. 10. Ratio of data free in MODIS SST products during 2003–2021. (a) Aqua_SST_Daytime. (b) Aqua_SST_Night. (c) Terra_SST_Daytime. (d) Terra_SST_Night.

with seasonal signals obviously as shown in Fig. 9, which expressed the unfixed relationship between SST and MAT in specific latitudinal zone. This could be caused by the movement of air and sea water. For instance, in the Southern Ocean, during the cold season (i.e., April–September), the influx of cold air from the south pole results in air temperatures that are lower than sea water temperatures, leading to an increased negative temperature difference. Conversely, during the warm season (i.e., October–March), the air is heated more intensely by solar radiation due to longer hours of sunshine while SSTs are cooler due to the diffusion of cold water melted from Antarctic glacial sea-ice, resulting in a greater positive temperature difference. Also, we examined the ratio of data coverage in SST products and found that variations in the high-latitude regions, such as West Coast of Africa and the West Coast of South America, are mainly caused by the coverage rate of SST. Not all SST products have available data due to cloud contamination and some other reasons. As shown in Fig. 10, the data coverage ratio in the daytime is generally larger than that at night especially
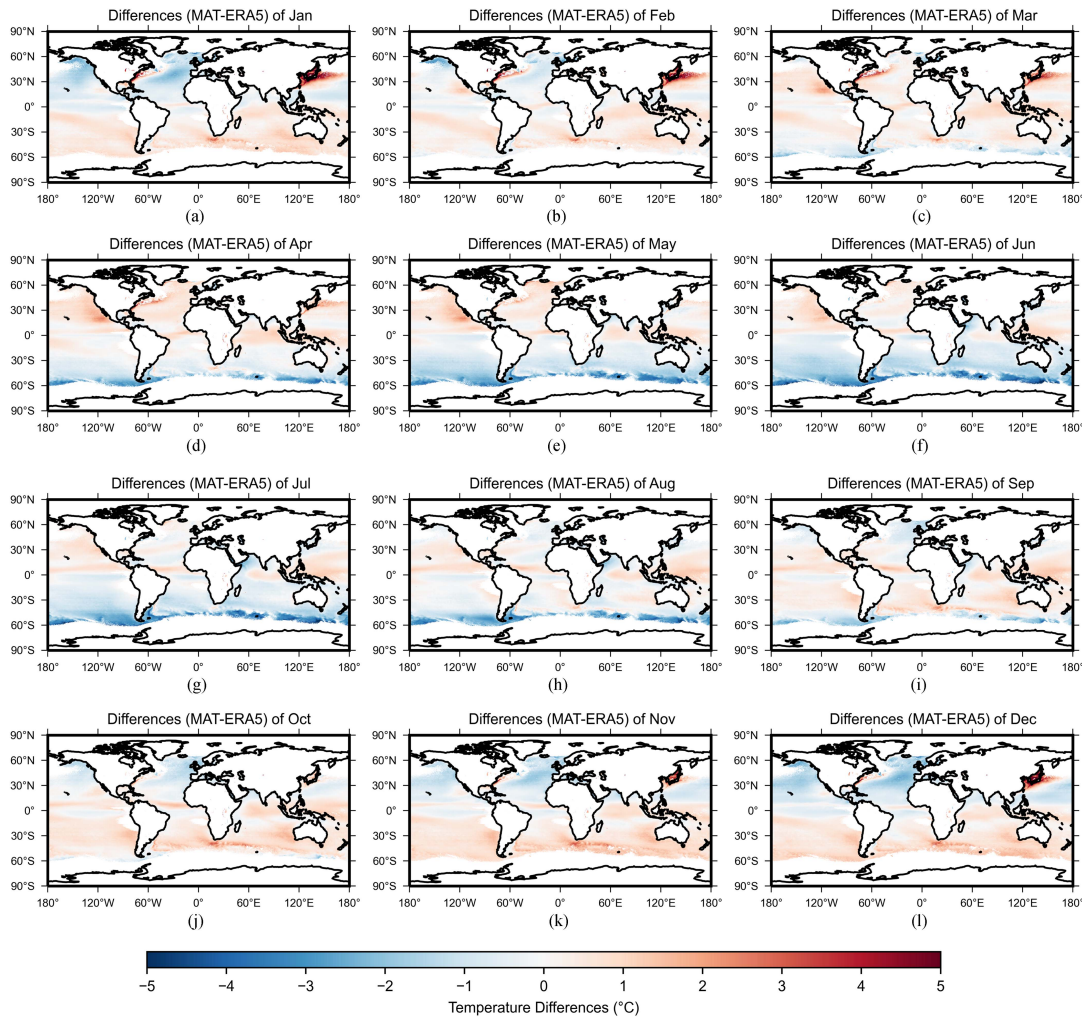
Fig. 11. Difference of average MAT and ERA5 of 2003–2021 for specific month. (a) Differences (MAT-ERA5) of January. (b) Differences (MAT-ERA5) of February. (c) Differences (MAT-ERA5) of March. (d) Differences (MAT-ERA5) of April. (e) Differences (MAT-ERA5) of May. (f) Differences (MAT-ERA5) of June. (g) Differences (MAT-ERA5) of July. (h) Differences (MAT-ERA5) of August. (i) Differences (MAT-ERA5) of September. (j) Differences (MAT-ERA5) of October. (k) Differences (MAT-ERA5) of November. (l) Differences (MAT-ERA5) of December.

in the south of the Alaska, the West Coast of Africa, and the West Coast of South America. Therefore, the averaged SSTs are merely containing the information of daytime SST product, which are much greater than MAT in these areas. Eventually, in order to obtain reliable results, the grids with data coverage ratio less than 95% were masked in the following analysis.

Likewise, Fig. 11 exhibits the difference map on a global scale between estimated MAT and ERA5 air temperature for specific month. MAT and ERA5 air temperature are highly comparable as they share the same physical definition. As shown in Fig. 11, significant deviations between ERA5 air temperature and estimated MAT are mainly located in the sea areas near eastern Asia and 60°S, whereas the deviations are smaller in most other regions. In addition, the occurrence of these deviations is highly related to seasons. For example, the deviation in eastern Asia mainly occurs in January, February, March, November, and December, which is during the Northern Hemisphere winter. However, the deviation in the sea area near 60°S mainly occurs in May, June, July, and August, which is during the Southern Hemisphere winter. The difference in the Southern Hemisphere is probably determined by the coverage of sea ice in this region.

Some studies have proved that ERA5 air temperature has a warm bias over sea ice in Arctic and Antarctic compared with buoys and weather stations [19], [20], which also happens in Fig. 12(a). In addition, in the Southern Hemisphere, the estimated MATs in the warm months, such as January, February, March, October, November, and December, are higher than ERA5 air temperature, whereas the estimated MAT values in the winter months (April–September) are lower than ERA5. The same pattern is observed in the Northern Hemisphere. This suggests that there are slight differences between ERA5 and estimated MAT in local details. However, on a larger spatial scale, the differences between the two are much smaller, as shown in Fig. 12. The comparison of latitudinal temperature in June and December reveals that the differences between ERA5 and MAT profile are small in most regions at the regional scale.

B. Warming Trend of Global Marine

1) Spatially Assessment of Warming Trend for Global Marine: The previous section has compared the difference between ERA5 air temperature and estimated MAT. This section will
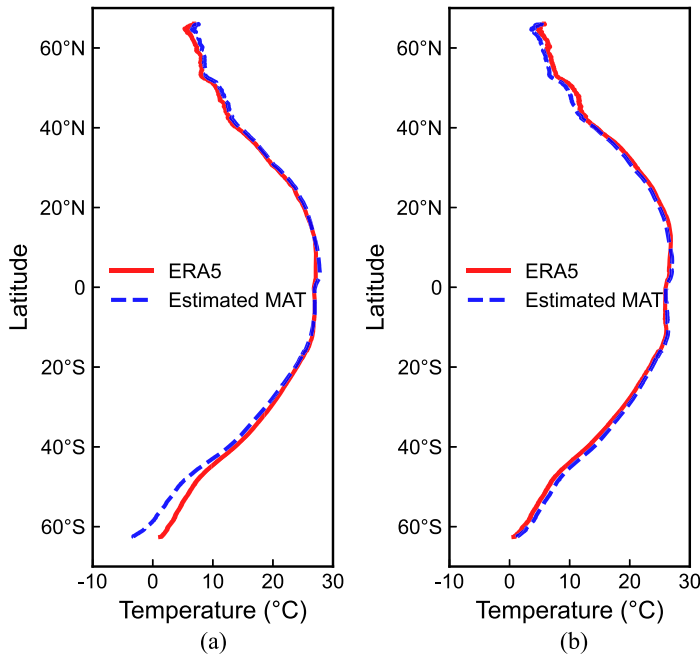
Fig. 12.   Mean temperature profiles of ERA5 and estimated MAT for (a) June and (b) December.

compare the difference between the two in capturing warming trend temporally and spatially. The warming trend is an important indicator for ocean climate change research. Due to the unevenness of solar radiation received by the Earth and the differences of circulation mode, warming trends probably vary in different places. Thus, the deviation of warming trend between ERA5 air temperature and the estimated MAT is compared spatially in Fig. 13. First, the warming trend profile at different latitudes is calculated from the averaged-temperature at the same latitude, as shown in Fig. 13(a). The result suggests that the fastest warming occurs in the sea areas near 40°N and 50°S, almost exceeding 0.025 °C/yr, whereas the warming trend of sea areas between 40°S and 20°N is relatively constant, around 0.02 °C/yr. At the same time, it also demonstrates that the trend of ERA5 air temperature and the estimated MAT is very close at most regions in terms of the deviation, except for the differences in the sea areas near 30°S and 10°N. This spatial pattern is similar to the study of Johnson and Lyman [64], with fast warming in Southern Ocean, Southern Pacific Ocean, and Southern Ocean. Moreover, other studies correlated to deeper ocean warming with depth greater than 1500 m also indirectly support this conclusion [65], [66], [67]. Therefore, it indicates that estimated MAT and ERA5 air temperature basically maintain consistency in expressing the warming trend at different-latitude sea areas. According to Fig. 13(b) and (c), temperature trends from both ERA5 and the estimated MAT exhibit the significant global ocean warming distributed in the western Pacific, western Atlantic, and northern Indian Ocean during 2003–2021. In summary, the warming trends derived from ERA5 air temperature set and estimated MAT are spatially close.

2) Temporally Assessment of Warming Trend for Global Marine: In addition, the warming trends of different regions were

calculated to better understand the regional warming variability during 2003–2021. Here, a straightforward numerical average of all grids cannot reflect the true warming rate at a regional scale, as the spherical shape of the Earth results in inequivalent area coverage in each grid at various latitudes. Therefore, an averaged regional temperature T should be calculated using an effective area-weighted method [68], [69], which can appropriately weight all grid cells in the region of interest based on their effective area coverage. This method can be expressed as follows:

$$T = \frac{\sum_{i=1}^{N} \cos\left(\mathrm{lat}_i \frac{\pi}{180}\right) T_i}{\sum_{i=1}^{N} \cos\left(\mathrm{lat}_i \frac{\pi}{180}\right)} \tag{6}$$

where N represents the total number of grid cells; T_i stands for the temperature of the grid cell i and lat_i stands for the latitude of the grid cell i.

Here, MAT, ERA5 air temperature, and the averaged SST are employed to temporally evaluate the warming rate of global marine. In this section, MAT and ERA5 product are used to assess the warming rate of air temperature on the ocean, whereas the averaged SST is used to assess the warming rate of sea water. Besides, to remove the uncertainties resulted from seasonal sea ice, the trend analysis was merely concentrated on the region range of 50°S–50°N and was nearly covered by liquid water annually. As shown in Fig. 14, satellite-based MAT is essentially consistent with ERA5 air temperature at both the regional and global scales. At global scale, the trend of MAT (0.017 ± 0.003 °C/yr) is just a little bit larger than that of ERA5 air temperature (0.016 ± 0.002 °C/yr) [see Fig. 14(a)], which is close to the result of UAHNMAT dataset [70]. Likewise, this phenomenon similarly happens at both the northern hemisphere and southern hemisphere [see Fig. 14(b) and (c)]. In contrast, the differences between SST and MAT are more significant. As displayed in Fig. 14(a), SST is about 1 °C higher than MAT and ERA5 air temperature on average, which is definitely consistent with the bias in Fig. 6(b). Besides, as shown in Fig. 14(a), the trends of air temperature from MAT and ERA5 air temperature are 0.017 ± 0.002 °C/yr and 0.016 ± 0.003 °C/yr, respectively, which are universally lower than that of SST (0.019 ± 0.003 °C/yr). Namely, the warming speed of SST is faster than that of MAT on a global scale.

From the perspective of regional difference, the warming trend is slower near the equator [see Fig. 14(d)] while faster in high-latitude regions [see Fig. 14(g) and (h)]. For example, the warming trends during the range of 30°S–50°S and 30°N–50°N both reach to 0.017 ± 0.003 °C/yr according to the trend of ERA5 air temperature. Notably, the warming trend during 10°S–30°S is the lowest one compared with that during 10°S–10°N and 30°S–50°S. This probably resulted from the changes of winds and eddies in the south hemisphere. It is well known that strong southeasterly winds dominate the current circulation in north region of 30°S, whereas the west-to-east prevailing westerly winds dominate the current circulation in south region of 30°S. This wind pattern creates positive wind stress rotations over almost the entire south hemisphere, especially between 10°S–45°S, driving anticyclonic subtropical circulation in each
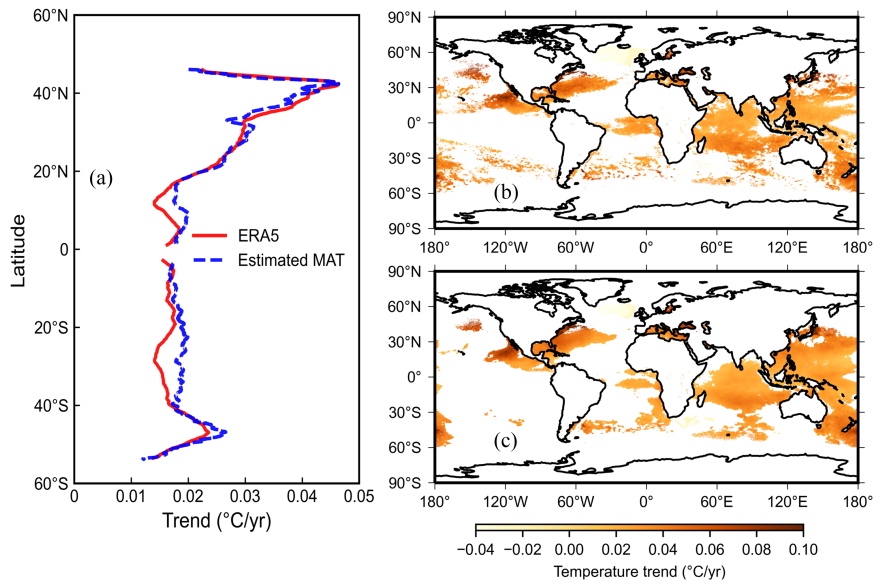
Fig. 13.   Warming trend comparison during 2003–2021 conducted by ERA5 data and estimated MAT in latitude band scale. (a) Trends derived from estimated MAT and ERA5 air temperature in varied latitudes. (b) Global warming trend derived from estimated MAT in grid scale. (c) Global warming trend derived from estimated ERA5 in grid scale. All of the trends have passed the P-test with $P < 0.05$.
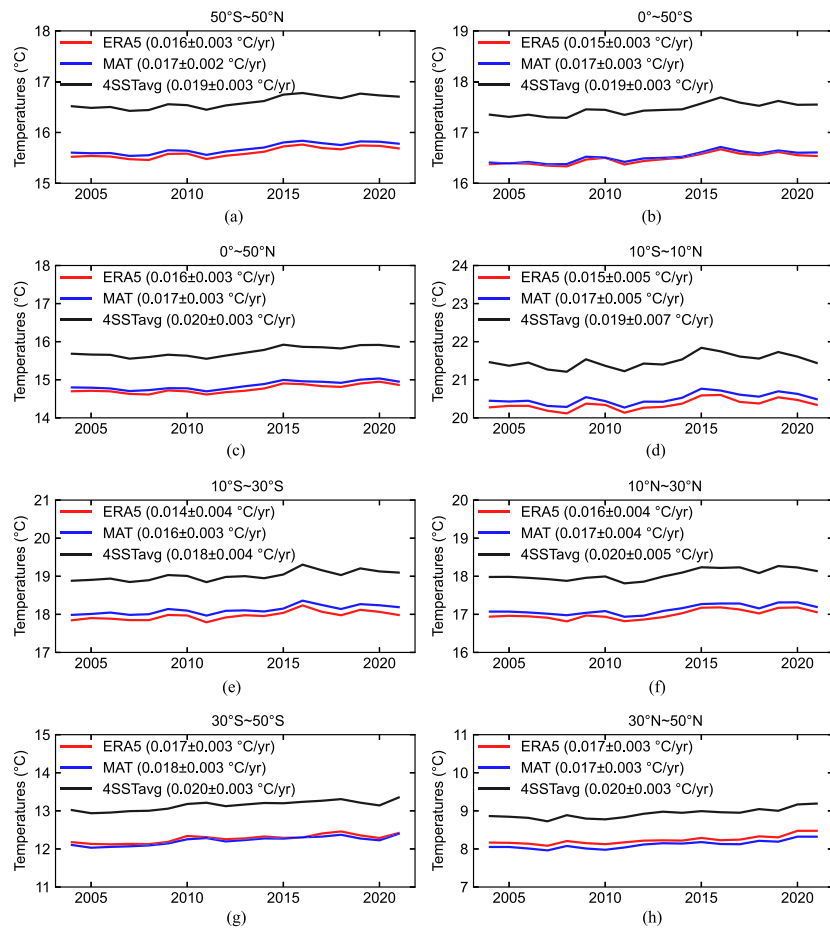

Fig. 14.   Warming trend comparison and analysis in different regional scale. And all of the trends have passed the P-test ($P < 0.05$). (a) 50°S–50°N. (b) 0°–50°S. (c) 0°–50°N. (d) 10°S–10°N. (e) 10°S–30°S. (f) 10°N–30°N. (g) 30°S–50°S. (h) 30°N–50°N.

ocean basin. Under the background of global climate warming, westerly winds are becoming stronger at high latitudes and the western boundary currents have penetrated poleward and are now transporting more heat into their extensions [71]. Ocean covers nearly 71% of the Earth's surface, and the rapid warming trend indicates that ocean has absorbed a lot of energy and heat, and simultaneously influenced the winds and currents in many regions especially in South Atlantic Ocean.

V. CONCLUSION

It has been undergoing a rapid warming worldwide since 1980s, which imposes a substantial impact on climatology and ecosystems. The warming contribution of ocean is a controversial issue remaining to be addressed in most occasions due to the limited numbers of observation stations that unmatched with the large area proportion. Reanalysis datasets, such as ERA5, are characterized with a sparse resolution and even the quality is strongly dominated by the observations assimilated in numerical models. Although numerous studies have been conducted to assess the quality of ERA5 air temperature dataset, there are still some uncertainties hard to quantify in those places where observations are sparse or even absent. In this research, we proposed a new approach to assess the performance of ERA5 air temperature grid by grid by incorporating rather limited in-situ MATs observed by buoys into remotely sensed SST product for the period of 2003–2021. During this assessment, a global monthly MAT product with spatial resolution of $0.05° \times 0.05°$ is produced with a stacked learning method of MLP. And this novel product was validated by in-situ observations, suggesting that the accuracy of the estimated MAT product (RMSE = $1.62\,°C$ and Bias = $-0.03\,°C$) is higher than that of averaged SSTs in validation results. Besides, the RMSE of 80.3% validation stations is located in the range of $0.5\,°C$–$2\,°C$, 2.6% less than $0.5\,°C$ and 19.7% greater than $2\,°C$ in the analysis of spatial accuracy, which makes it a credible reference for ERA5 air temperature assessment on the ocean. Eventually, it has been proved that ERA5 air temperature is consistent with estimated MAT not only on spatio-temporal continuity but also on the warming trend of global ocean. Both of the datasets exhibit the significant warming in the western Pacific, western Atlantic, and northern Indian Ocean. In addition, as the analysis reported that the warming amplitude of SST ($0.019 \pm 0.003\,°C/yr$) is greater than that of ERA5 air temperature ($0.016 \pm 0.003\,°C/yr$) in range of 50°S–50°N, where it is definitely covered by liquid sea water. Namely, it will lead to overestimation of warming amplitude if only taking warming rate of SST into consideration in warming assessment. However, the fusion of multisource data, including in-situ observations, remotely sensed product, and model-based simulations, can improve the accuracy of ocean temperature and propose a robust and effective approach to understand real situation about global climate change on the ocean.

REFERENCES

[1] D. Laffoley and J. M. Baxter, *Explaining Ocean Warming: Causes, Scale, Effects and Consequences*. Gland, Switzerland: IUCN, 2016.

[2] J.-J. Luo, W. Sasaki, and Y. Masumoto, "Indian Ocean warming modulates Pacific climate change," *Proc. Nat. Acad. Sci.*, vol. 109, no. 46, pp. 18701–18706, 2012, doi: 10.1073/pnas.1210239109.

[3] R. D. Cess and S. D. Goldenberg, "The effect of ocean heat capacity upon global warming due to increasing atmospheric carbon dioxide," *J. Geophys. Res.-Oceans*, vol. 86, no. C1, pp. 498–502, Jan. 1981, doi: 10.1029/JC086iC01p00498.

[4] X. Yang and P. Huang, "Restored relationship between ENSO and Indian summer monsoon rainfall around 1999/2000," *Innovation*, vol. 2, no. 2, 2021, Art. no. 100102.

[5] E. C. Kent and J. J. Kennedy, "Historical estimates of surface marine temperatures," *Annu. Rev. Mar. Sci.*, vol. 13, pp. 283–311, 2021.

[6] P. D. Jones, M. New, D. E. Parker, S. Martin, and I. G. Rigor, "Surface air temperature and its changes over the past 150 years," *Rev. Geophys.*, vol. 37, no. 2, pp. 173–199, May 1999.

[7] C. K. Folland, D. E. Parker, and F. E. Kates, "Worldwide marine temperature fluctuations 1856–1981," *Nature*, vol. 310, no. 5979, pp. 670–673, 1984.

[8] P. D. Jones et al., "Evidence for global warming in the past decade," *Nature*, vol. 332, no. 6167, pp. 790–790, Apr. 1988, doi: 10.1038/332790b0.

[9] R. J. Millar et al., "Emission budgets and pathways consistent with limiting warming to 1.5 °C," *Nature Geosci.*, vol. 10, no. 10, pp. 741–747, Oct. 2017, doi: 10.1038/ngeo3031.

[10] E. C. Kent et al., "Global analysis of night marine air temperature and its uncertainty since 1880: The HadNMAT2 data set," *J. Geophys. Res.-Atmos.*, vol. 118, no. 3, pp. 1281–1298, Feb. 2013, doi: 10.1002/jgrd.50152.

[11] K. Cowtan et al., "Robust comparison of climate models with observations using blended land air and ocean sea surface temperatures," *Geophys. Res. Lett.*, vol. 42, no. 15, pp. 6526–6534, Aug. 2015.

[12] M. Richardson, K. Cowtan, E. Hawkins, and M. B. Stolpe, "Reconciled climate response estimates from climate models and the energy budget of Earth," *Nature Climate Change*, vol. 6, no. 10, pp. 931–935, Oct. 2016.

[13] J. R. Christy, D. E. Parker, S. J. Brown, I. Macadam, M. Stendel, and W. B. Norris, "Differential trends in tropical sea surface and atmospheric temperatures since 1979," *Geophys. Res. Lett.*, vol. 28, no. 1, pp. 183–186, 2001.

[14] I. Khalil, P. M. Atkinson, and P. Challenor, "Looking back and looking forwards: Historical and future trends in sea surface temperature (SST) in the Indo-Pacific region from 1982 to 2100," *Int. J. Appl. Earth Observ. Geoinf.*, vol. 45, pp. 14–26, Mar. 2016.

[15] E. Freeman et al., "ICOADS release 3.0: A major update to the historical marine climate record," *Int. J. Climatol.*, vol. 37, no. 5, pp. 2211–2232, Apr. 2017.

[16] S. J. Worley, S. D. Woodruff, R. W. Reynolds, S. J. Lubker, and N. Lott, "ICOADS release 2.1 data and products," *Int. J. Climatol.*, vol. 25, no. 7, pp. 823–842, Jun. 2005.

[17] H. Hersbach et al., "The ERA5 global reanalysis," *Quart. J. Roy. Meteorol. Soc.*, vol. 146, no. 730, pp. 1999–2049, Jul. 2020.

[18] F. Mesinger et al., "North American regional reanalysis," *Bull. Amer. Meteorol. Soc.*, vol. 87, no. 3, pp. 343–360, Mar. 2006.

[19] C. Wang, R. M. Graham, K. Wang, S. Gerland, and M. A. Granskog, "Comparison of ERA5 and ERA-interim near-surface air temperature, snowfall and precipitation over Arctic sea ice: Effects on sea ice thermodynamics and evolution," *Cryosphere*, vol. 13, no. 6, pp. 1661–1679, 2019.

[20] J. Zhu, A. Xie, X. Qin, Y. Wang, B. Xu, and Y. Wang, "An assessment of ERA5 reanalysis for Antarctic near-surface air temperature," *Atmosphere*, vol. 12, no. 2, 2021, Art. no. 217.

[21] J. A. Sobrino, Y. Julien, J. C. Jimenez-Munoz, D. Skokovic, and G. Soria, "Near real-time estimation of sea and land surface temperature for MSG SEVIRI sensors," *Int. J. Appl. Earth Observ. Geoinf.*, vol. 89, Jul. 2020, Art. no. 102096.

[22] C. Walton, W. Pichel, J. Sapper, and D. May, "The development and operational application of nonlinear algorithms for the measurement of sea surface temperatures with the NOAA polar-orbiting environmental satellites," *J. Geophys. Res.-Oceans*, vol. 103, no. C12, pp. 27999–28012, 1998.

[23] A. Rubino, D. Zanchettin, F. De Rovere, and M. J. McPhaden, "On the interchangeability of sea-surface and near-surface air temperature anomalies in climatologies," *Sci. Rep.*, vol. 10, no. 1, May 2020, Art. no. 7433.

[24] E. J. Good, D. J. Ghent, C. E. Bulgin, and J. J. Remedios, "A spatiotemporal analysis of the relationship between near-surface air temperature and satellite land surface temperatures using 17 years of data from the ATSR series," *J. Geophys. Res.-Atmos.*, vol. 122, no. 17, pp. 9185–9210, Sep. 2017.

[25] X. Lin et al., "Empirical estimation of near-surface air temperature in China from MODIS LST data by considering physiographic features," *Remote Sens.*, vol. 8, no. 8, 2016, Art. no. 629.

[26] D. Mutiibwa, S. Strachan, and T. Albright, "Land surface temperature and surface air temperature in complex terrain," *IEEE J. Sel. Topics Appl. Earth Observ. Remote Sens.*, vol. 8, no. 10, pp. 4762–4774, Oct. 2015.

[27] J. Hooker, G. Duveiller, and A. Cescatti, "A global dataset of air temperature derived from satellite remote sensing and weather stations," *Sci. Data*, vol. 5, no. 1, Nov. 2018, Art. no. 180246.

[28] Y. H. Rao et al., "Estimating daily average surface air temperature using satellite land surface temperature and top-of-atmosphere radiation products over the Tibetan Plateau," *Remote Sens. Environ.*, vol. 234, Dec. 2019, Art. no. 111462.

[29] H. Shen, Y. Jiang, T. Li, Q. Cheng, C. Zeng, and L. Zhang, "Deep learning-based air temperature mapping by fusing remote sensing, station, simulation and socioeconomic data," *Remote Sens. Environ.*, vol. 240, Apr. 2020, Art. no. 111692.

[30] B. Huang et al., "Improvements of the daily optimum interpolation sea surface temperature (DOISST) version 2.1," *J. Climate*, vol. 34, no. 8, pp. 2923–2939, 2021.

[31] J. J. Kennedy, N. A. Rayner, C. P. Atkinson, and R. E. Killick, "An ensemble data set of sea surface temperature change from 1850: The Met Office Hadley Centre HadSST.4.0.0.0 data set," *J. Geophys. Res.-Atmos.*, vol. 124, no. 14, pp. 7719–7763, Jul. 2019.

[32] M. Ishii, A. Shouji, S. Sugimoto, and T. Matsumoto, "Objective analyses of sea-surface temperature and marine meteorological variables for the 20th century using ICOADS and the Kobe collection," *Int. J. Climatol.*, vol. 25, no. 7, pp. 865–879, Jun. 2005, doi: 10.1002/joc.1169.

[33] A. Al-Yaari et al., "Global-scale evaluation of two satellite-based passive microwave soil moisture datasets (SMOS and AMSR-E) with respect to land data assimilation system estimates," *Remote Sens. Environ.*, vol. 149, pp. 181–195, Jun. 2014.

[34] C. L. Gentemann, T. Meissner, and F. J. Wentz, "Accuracy of satellite sea surface temperatures at 7 and 11 GHz," *IEEE Trans. Geosci. Remote Sens.*, vol. 48, no. 3, pp. 1009–1018, Mar. 2010.

[35] F. J. Wentz, C. L. Gentemann, and K. Hilburn, "Three years of ocean products from AMSR-E: Evaluation and applications," in *Proc. IEEE 25th Int. Geosci. Remote Sens. Symp.*, 2005, pp. 4929–4932.

[36] I. J. Barton, "Satellite-derived sea surface temperatures: Current status," *J. Geophys. Res.-Oceans*, vol. 100, no. C5, pp. 8777–8790, May 1995.

[37] S. García-Monteiro et al., "A comparison between satellite and in situ SST data on a global scale," *Fifth Recent Advances in Quantitative Remote Sensing*. Torrent, Spain, Dec. 2018, p. 254.

[38] N. A. Rayner et al., "Global analyses of sea surface temperature, sea ice, and night marine air temperature since the late nineteenth century," *J. Geophys. Res.-Atmos.*, vol. 108, no. D14, Jul. 2003, Art. no. 4407.

[39] R. W. Reynolds, N. A. Rayner, T. M. Smith, D. C. Stokes, and W. Wang, "An improved in situ and satellite SST analysis for climate," *J. Climate*, vol. 15, no. 13, pp. 1609–1625, 2002.

[40] R. W. Reynolds, T. M. Smith, C. Liu, D. B. Chelton, K. S. Casey, and M. G. Schlax, "Daily high-resolution-blended analyses for sea surface temperature," *J. Climate*, vol. 20, no. 22, pp. 5473–5496, 2007.

[41] E. K. Fiedler et al., "Intercomparison of long-term sea surface temperature analyses using the GHRSST multi-product ensemble (GMPE) system," *Remote Sens. Environ.*, vol. 222, pp. 18–33, 2019.

[42] M. Martin et al., "Group for high resolution sea surface temperature (GHRSST) analysis fields inter-comparisons. Part 1: A GHRSST multi-product ensemble (GMPE)," *Deep Sea Res. Part II: Topical Stud. Oceanogr.*, vol. 77, pp. 21–30, 2012.

[43] S. Good et al., "The current configuration of the OSTIA system for operational production of foundation sea surface temperature and ice concentration analyses," *Remote Sens.*, vol. 12, no. 4, 2020, Art. no. 720.

[44] T. M. Chin, J. Vazquez-Cuervo, and E. M. Armstrong, "A multi-scale high-resolution analysis of global sea surface temperature," *Remote Sens. Environ.*, vol. 200, pp. 154–169, Oct. 2017.

[45] Z. Hausfather, K. Cowtan, D. C. Clarke, P. Jacobs, M. Richardson, and R. Rohde, "Assessing recent warming using instrumentally homogeneous sea surface temperature records," *Sci. Adv.*, vol. 3, no. 1, 2017, Art. no. e1601207.

[46] B. Huang, C. Liu, E. Freeman, G. Graham, T. Smith, and H.-M. Zhang, "Assessment and intercomparison of NOAA daily optimum interpolation sea surface temperature (DOISST) version 2.1," *J. Climate*, vol. 34, no. 18, pp. 7421–7441, 2021.

[47] B. Bell et al., "The ERA5 global reanalysis: Preliminary extension to 1950," *Quart. J. Roy. Meteorol. Soc.*, vol. 147, no. 741, pp. 4186–4227, Oct. 2021.

[48] Y. He, C. Chen, B. Li, and Z. Zhang, "Prediction of near-surface air temperature in glacier regions using ERA5 data and the random forest regression method," *Remote Sens. Appl.: Soc. Environ.*, vol. 28, Nov. 2022, Art. no. 100824.

[49] M. Yilmaz, "Accuracy assessment of temperature trends from ERA5 and ERA5-land," *Sci. Total Environ.*, vol. 856, Jan. 2023, Art. no. 159182.

[50] J. Zou et al., "Performance of air temperature from ERA5-Land reanalysis in coastal urban agglomeration of Southeast China," *Sci. Total Environ.*, vol. 828, Jul. 2022, Art. no. 154459.

[51] B. McNicholl, Y. H. Lee, A. G. Campbell, and S. Dev, "Evaluating the reliability of air temperature from ERA5 reanalysis data," *IEEE Geosci. Remote Sens. Lett.*, vol. 19, Jan. 2022, Art. no. 1004505.

[52] Y. N. Yu, W. X. Xiao, Z. L. Zhang, X. Cheng, F. M. Hui, and J. C. Zhao, "Evaluation of 2-m air temperature and surface temperature from ERA5 and ERA-I using buoy observations in the Arctic during 2010–2020," *Remote Sens.*, vol. 13, no. 14, Art. no. 2813, Jul. 2021.

[53] E. Dutra, J. Munoz-Sabater, S. Boussetta, T. Komori, S. Hirahara, and G. Balsamo, "Environmental lapse rate for high-resolution land surface downscaling: An application to ERA5," *Earth Space Sci.*, vol. 7, no. 5, May 2020, Art. no. e2019EA000984.

[54] C. H. Karaman and Z. Akyurek, "Evaluation of near-surface air temperature reanalysis datasets and downscaling with machine learning based random forest method for complex terrain of Turkey," *Adv. Space Res.*, vol. 71, no. 12, pp. 5256–5281, Jun. 2023.

[55] X. Wang, V. Tolksdorf, M. Otto, and D. Scherer, "WRF-based dynamical downscaling of ERA5 reanalysis data for High Mountain Asia: Towards a new version of the High Asia Refined analysis," *Int. J. Climatol.*, vol. 41, no. 1, pp. 743–762, Jan. 2021.

[56] G. J. Marshall, "Trends in Antarctic geopotential height and temperature: A comparison between radiosonde and NCEP-NCAR reanalysis data," *J. Climate*, vol. 15, no. 6, pp. 659–674, 2002.

[57] Y. Yang, Q. X. Li, Z. Y. Song, W. B. Sun, and W. J. Dong, "A comparison of global surface temperature variability, extremes and warming trend using reanalysis datasets and CMST-interim," *Int. J. Climatol.*, vol. 42, no. 11, pp. 5609–5628, Sep. 2022.

[58] C. Donlon et al., "The global ocean data assimilation experiment high-resolution sea surface temperature pilot project," *Bull. Amer. Meteorol. Soc.*, vol. 88, no. 8, pp. 1197–1214, 2007.

[59] Y. Hao, T. Cui, V. Singh, J. Zhang, R. Yu, and Z. Zhang, "Validation of MODIS sea surface temperature product in the coastal waters of the Yellow Sea," *IEEE J. Sel. Topics Appl. Earth Observ. Remote Sens.*, vol. 10, no. 5, pp. 1667–1680, May 2017.

[60] M. Belgiu and L. Dragut, "Random forest in remote sensing: A review of applications and future directions," *Int. Soc. Photogrammetry Remote Sens. J.*, vol. 114, pp. 24–31, Apr. 2016.

[61] J. R. Quinlan, "Learning with continuous classes," in *Proc. 5th Australian Joint Conf. Artif. Intell.*, 1992, vol. 92, pp. 343–348.

[62] P. T. Noi, J. Degener, and M. Kappas, "Comparison of multiple linear regression, cubist regression, and random forest algorithms to estimate daily air surface temperature from dynamic combinations of MODIS LST data," *Remote Sens.*, vol. 9, no. 5, 2017, Art. no. 398.

[63] W. L. Smith et al., "Observations of the infrared radiative properties of the ocean–Implications for the measurement of sea surface temperature via satellite remote sensing," *Bull. Amer. Meteorol. Soc.*, vol. 77, no. 1, pp. 41–51, Jan. 1996.

[64] G. C. Johnson and J. M. Lyman, "Warming trends increasingly dominate global ocean," *Nature Climate Change*, vol. 10, no. 8, pp. 757–761, Aug. 2020.

[65] W. J. Cai et al., "Southern ocean warming and its climatic impacts," *Sci. Bull.*, vol. 68, no. 9, pp. 946–960, May 2023.

[66] L. J. Cheng et al., "Past and future ocean warming," *Nature Rev. Earth Environ.*, vol. 3, no. 11, pp. 776–794, Nov. 2022.

[67] H. Su, Y. A. Wei, W. F. Lu, X. H. Yan, and H. S. Zhang, "Unabated global ocean warming revealed by ocean heat content from remote sensing reconstruction," *Remote Sens.*, vol. 15, no. 3, Feb. 2023, Art. no. 566.

[68] I. Harris, P. D. Jones, T. J. Osborn, and D. H. Lister, "Updated high-resolution grids of monthly climatic observations—The CRU TS3.10 dataset," *Int. J. Climatol.*, vol. 34, no. 3, pp. 623–642, 2014.

[69] K. Wang et al., "Continuously amplified warming in the Alaskan Arctic: Implications for estimating global warming hiatus," *Geophys. Res. Lett.*, vol. 44, no. 17, pp. 9029–9038, 2017.

[70] R. A. Junod and J. R. Christy, "A new compilation of globally gridded night-time marine air temperatures: The UAHNMATv1 dataset," *Int. J. Climatol.*, vol. 40, no. 5, pp. 2609–2623, Apr. 2020.

[71] J. Li, M. Roughan, and C. Kerry, "Drivers of ocean warming in the western boundary currents of the Southern Hemisphere," *Nature Climate Change*, vol. 12, no. 10, pp. 901–909, Oct. 2022.

Ning Lu received the B.S. and M.S. degrees in cartography and geographical information system from the China University of Geosciences, Wuhan, China, in 2003 and 2006, respectively, and the Ph.D. degree in cartography and geographical information system from the Institute of Geographic Sciences and Natural Resources Research, Chinese Academy of Sciences, Beijing, China, in 2009.

His research interests include environmental remote sensing and its climate analysis applications.

Min He received the B.S. degree in cartography and geographical information system from the Southwest University, Chongqing, China, in 2014, and the M.S. degree in surveying and mapping engineering from Aerospace Information Research Institute, Chinese Academy of Sciences, Beijing, China, in 2018. She is currently working toward the Ph.D. degree in cartography and geographical information system with the Institute of Geographic Sciences and Natural Resources Research, Chinese Academy of Sciences.

Her research interests include satellite-based leaf area index retrieval and reconstruction of near surface air temperature.

Ling Yao received the B.S. and M.S. degrees in cartography and geographical information system from Nanjing Normal University, Nanjing, China, in 2004 and 2009, respectively, and the Ph.D. degree in cartography and geographical information system from the Institute of Geographic Sciences and Natural Resources Research, Chinese Academy of Sciences, Beijing, China, in 2012.

His research interests include remote sensing Big Data analytics and applications of GIS.

Jun Qin received the B.S. degree in meteorology from Nanjing Institute of Meteorology, Nanjing, China, in 2001, and the Ph.D. degree in remote sensing and geographic information systems from Beijing Normal University, Beijing, China, in 2006.

His current research interests include retrieving land surface parameters from remote sensing data, land surface process modeling, land surface data assimilation, and optimization algorithms.